



INTEGRATION OF NOVEL STACK COMPONENTS FOR PERFORMANCE, IMPROVED DURABILITY AND LOWER COST

Grant agreement no.: 700127

Start date: 01.05.2016 – Duration: 36 months

Project Coordinator: Johnson Matthey plc

DELIVERABLE REPORT

D4.5 – PRODUCE A MODEL OF DEGRADATION AND PHYSICAL CHANGES TO CATALYST LAYER STRUCTURE DURING AGEING

| | | |
|------------------------------|---|--|
| Due Date | 31 st January 2019 | |
| Author(s) | Jonathan Sharman, Adam Hodgkinson, Alex Martinez Bonastre, Friedemann Hegge, Severin Vierrath, Silvain Buche, Carol Wayne | |
| Work Package | 4 | |
| Work Package Leader | JMFC | |
| Lead Beneficiary | ALU-FR (IMTEK) | |
| Date released by WP Leader | 12/02/2019 | |
| Date released by Coordinator | 14/02/2019 | |

DISSEMINATION LEVEL

| | | |
|-----------|--|----------|
| PU | <i>Public</i> | X |
| PP | <i>Restricted to other programme participants (including the Commission Services)</i> | |
| RE | <i>Restricted to a group specified by the consortium (including the Commission Services)</i> | |
| CO | <i>Confidential, only for members of the consortium (including the Commission Services)</i> | |

NATURE OF THE DELIVERABLE

| | | |
|----------|---------------------|----------|
| R | <i>Report</i> | X |
| P | <i>Prototype</i> | |
| D | <i>Demonstrator</i> | |
| O | <i>Other</i> | |

| D4.5 – SUMMARY | |
|--|---|
| Keywords | Fuel cell model, catalyst support ageing, carbon corrosion |
| Full Abstract (Confidential) | A model has been developed that is simple to use but incorporates the critical parameters that allow a reliable prediction of the impact of catalyst support ageing on performance. The model uses various parameters, such as catalyst layer thickness, porosity and roughness factor as the inputs and then calculates the total over-potential using electrochemical kinetic and mass transport resistance data. Structural effects are included by integrating data from 3D-reconstructions of the catalyst layer that are derived from FIB-SEM tomography. Validation against in-cell degradation has shown that the model gives a good prediction of performance decay. In the stress tests used for this work, the major contributor to the performance loss was the increased mass transport resistance due to a loss of active catalyst (Pt) surface area, rather than from substantial layer structural change. |
| Publishable Abstract (If different from above) <i>For publication on website</i> | |

| REVISIONS | | | |
|------------------|-------------|-------------------|-----------------|
| Version | Date | Changed by | Comments |
| | | | |
| | | | |

D4.5 – PRODUCE A MODEL OF DEGRADATION AND PHYSICAL CHANGES TO CATALYST LAYER STRUCTURE DURING AGEING

CONTENTS

| | | |
|-------|--|----|
| 1 | Glossary | 4 |
| 1.1 | Abbreviations | 4 |
| 1.2 | Symbols | 4 |
| 1.3 | Constants | 4 |
| 2 | Introduction..... | 5 |
| 3 | Experimental | 5 |
| 3.1 | Accelerated Stress Tests | 5 |
| 3.2 | Tomography..... | 5 |
| 3.3 | Parameter calculation | 6 |
| 3.4 | Electrochemical measurements..... | 6 |
| 3.5 | Model implementation | 6 |
| 4 | Results and Discussion | 7 |
| 4.1 | Experimental results | 7 |
| 4.1.1 | Performance loss | 7 |
| 4.1.2 | Structural changes | 8 |
| 4.2 | General description of the model..... | 9 |
| 4.3 | Model results: MTR as a function of..... | 11 |
| 4.3.1 | Pore space (tortuosity, Porosity, Thickness) | 11 |
| 4.3.2 | ECSA loss..... | 12 |
| 4.3.3 | Wetting behavior: contact angle | 13 |
| 4.3.4 | Ionomer film thickness | 13 |
| 4.4 | Validating the Model..... | 14 |
| 5 | Conclusions..... | 15 |
| 6 | Recommendations and Future Work | 15 |
| 7 | References | 15 |

1 GLOSSARY

1.1 ABBREVIATIONS

| ABBREVIATION | EXPLANATION |
|--------------|------------------------------|
| BV | Butler-Volmer |
| CL | Catalyst layer |
| GDL | Gas diffusion layer |
| ECSA | Electrochemical surface area |
| EQ | Equilibrium |
| MTR | Mass transport resistance |
| RF | Roughness factor |

1.2 SYMBOLS

| SYMBOL | UNIT | DENOMINATION |
|-----------------|-------------------|--|
| U | V | Cell voltage |
| E_0 | V | Equilibrium potential |
| η_{kin} | V | Kinetic overpotential |
| η_{MTR} | V | Overpotential of the mass transport resistance |
| ϕ_{ohmic} | Ω | Ohmic resistance |
| c_{O_2} | $\frac{mol}{m^3}$ | Oxygen concentration |
| T | K | Temperature |
| t | m | Thickness (film, GDL, CL) |
| s | - | Saturation |
| j_{O_2} | $\frac{mol}{s}$ | Oxygen molar flux |
| κ_{H_2O} | m^2 | Intrinsic permeability |
| q_{H_2O} | $\frac{m^3}{s}$ | Water volume flux |

1.3 CONSTANTS

| SYMBOL | VALUE | DENOMINATION |
|---------------|--------------------------------|--|
| α | 0.5 | Symmetry factor |
| R | $8.315 \frac{J}{mol K}$ | Ideal gas constant |
| F | $96\,485.3329 \frac{A}{mol}$ | Faraday constant |
| H | $2.5 * 10^5 Pa m^3 mol^{-1}$ | Henry constant at 80 °C, 80 % RH ^[1] |
| $R_{O_2,if}$ | $1000 \frac{s}{m}$ | Interfacial oxygen resistance at ionomer film ^[1] |
| D_{film} | $5.9 * 10^{-11} \frac{m^2}{s}$ | Bulk oxygen diffusion coefficient of ionomer thin film at at 80 °C, 80 % RH ^[1] |
| M_{H_2O} | $18 * 10^{-3} \frac{kg}{mol}$ | Molar mass of water |
| μ_{H_2O} | $354.49 * 10^{-6} Pa s$ | Dynamic viscosity of water |
| ρ_{H_2O} | $971.79 kg m^{-3}$ | Density of water |

2 INTRODUCTION

The overall goal of this deliverable was to quantify the physical changes taking place in the cathode catalyst layer during stability testing and to set up a model that reflects the impact of degradation on overall cell performance. The work therefore includes ageing via accelerated stress tests (ASTs), investigation of structural changes via FIB-SEM (focused ion beam – scanning electron microscope) tomography and electrochemical experiments, as well as the setting up of the model according to the experimental insights. In early tests, accelerated ageing of cathode catalyst layers had shown significant performance degradation and this work set out to understand the causes of this performance loss, in terms of physical and chemical changes.

3 EXPERIMENTAL

In the following sections, the methods and samples are described briefly. In order to produce the model, samples were first aged (Section 3.1) and then investigated for structural changes of the cathode catalyst layer by tomography (Sections 3.2 and 3.3). In electrochemical measurements (Section 3.4), performance decay was quantified. Finally, a model was implemented (Section 3.5).

3.1 ACCELERATED STRESS TESTS

The cell and stand were commissioned using the INSPIRE baseline catalyst layers laminated on to Nafion NRE 211 membranes. A series of samples were produced for characterisation following the DOE catalyst support cycling protocol^[2], which cycles the voltage between 1.0 and 1.5 V at 500 mV/s in a hydrogen / nitrogen environment and is expected to lead to carbon support corrosion for susceptible materials. Samples were subjected to 100, 500 and 1000 cycles and the performance losses were characterised by measuring air polarisation curves and active catalyst surface area using cyclic voltammetry. 1000 cycles was chosen as the maximum number of cycles as the voltage loss observed at that point already exceeded the limit given by the DOE of 30 mV at 1.5 A/cm².

3.2 TOMOGRAPHY

FIB-SEM (focused ion beam – scanning electron microscope) tomography was chosen to capture the degradation via physical changes. With a resolution of a few nanometres and the ability to image areas a few microns wide, FIB-SEM proved to be the most suitable technique to resolve small changes in representative volumes of the catalyst layer microstructure. The process of obtaining a 3D-representation of a microstructure involves image acquisition, geometrical alignments and segmentation (Figure 1). In the acquisition, an image stack is generated by alternating FIB milling and SEM imaging. The image stack is then aligned and segmented yielding a 3D representation of the physical structure. The segmentation, i.e. discrimination between pores and solid, is crucial for subsequent calculation of parameters and is not straightforward. To enhance the contrast between the pores and the solid material, an infiltration via atomic layer deposition of ZnO was developed at IMTEK. This method of enhancing contrast has, for the first time, allowed semi-automatic segmentation of the datasets such that the time needed for segmentation can be reduced by a factor of ten. The structural information is then available as a matrix of ones and zeros representing bulk material and pore space.

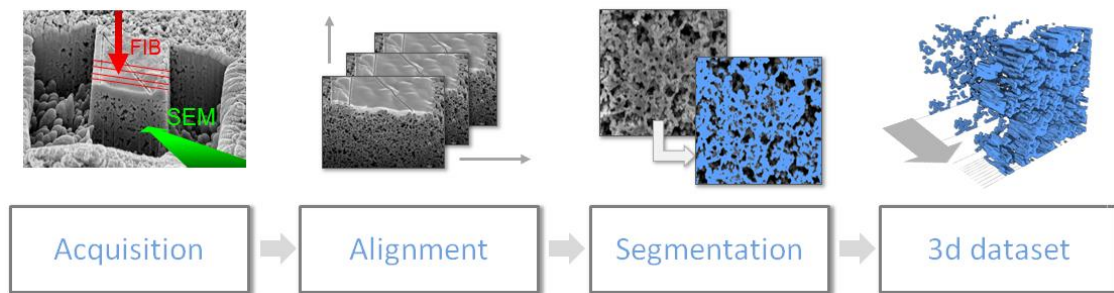


Figure 1: Process flow chart of FIB-SEM tomography

3.3 PARAMETER CALCULATION

Once the 3D structures had been rendered, structural parameters were calculated. The layer thickness can be easily extracted from the datasets. The porosity was calculated as the mean of the matrix. The diffusivity was calculated with the DiffuDict module of GeoDict. The pore sizes of the catalyst layer lay in the range of the mean free path length of the diffusing oxygen and water; thus, diffusive gas transport is governed both by interparticle collision (Laplace diffusion) and wall collisions (Knudsen diffusion) in similar amounts. The diffusion coefficient was, therefore, calculated by the Bosanquet approximation [3].

3.4 ELECTROCHEMICAL MEASUREMENTS

All electrochemical measurements were performed in a single cell of 5 cm² serpentine flow field with a Scribner 850e fuel cell testing system. The active area of the cells was reduced to 1 cm² to create 'differential conditions', meaning that no significant variation in reactant or product concentration occurs across the active area. Polarisation curves were recorded under H₂/air with flows of 0.2/0.5 slpm respectively at 80°C, 80% relative humidity and an absolute pressure of 1.5 bar (in accordance with the DOE protocol). The electrochemically active surface area (ECSA) was measured using cyclic voltammetry (CV). The CV was conducted under H₂/N₂ with flows of 0.2/0 slpm at 80°C, 100% relative humidity and ambient pressure.

Limiting current measurements were performed in two setups: a) in normal H₂/air operation and b) in H₂-pumping mode. The H₂-pumping mode allows mass transport to be assessed with no liquid water present in the cathode catalyst layer, as no water is being generated in the catalyst layer whilst pumping H₂. The H₂-pumping was conducted according to Spingler et al. [4] with 0.1% H₂ in Ar on the working electrode (cathode) and 2% H₂ in Ar on the counter electrode (anode), hydrogen being pumped from the cathode catalyst layer to the anode catalyst layer. The limiting current was measured at 5, 50 and 100 kPa backpressure, 80°C and 80% relative humidity. The limiting current under H₂/air operation was measured at the normal polarisation conditions and a voltage of 0.1 V.

3.5 MODEL IMPLEMENTATION

The model was implemented in Matlab as simple m-functions: one to calculate the mass transport overpotential and one for polarisation curve prediction. The results from the tomography, and data from electrochemical characterisation, served as inputs to the model. The model was validated by comparing the measured performance loss to the simulated performance loss, considering the change of catalyst support structure and active surface area. Using sensitivity studies, as described in Section 4.3, the cause of the performance loss related to carbon corrosion of the catalyst support was investigated.

4 RESULTS AND DISCUSSION

4.1 EXPERIMENTAL RESULTS

4.1.1 PERFORMANCE LOSS

As can be seen in Figure 2, there is little performance loss after 100 cycles for any current density, while after 1000 cycles the performance shows significant losses across most of the curve. At the reference current density of 1.5 A/cm² the aged cell shows an overpotential of 140 mV compared to the pristine cell, significantly exceeding the DOE target of only 30 mV loss.

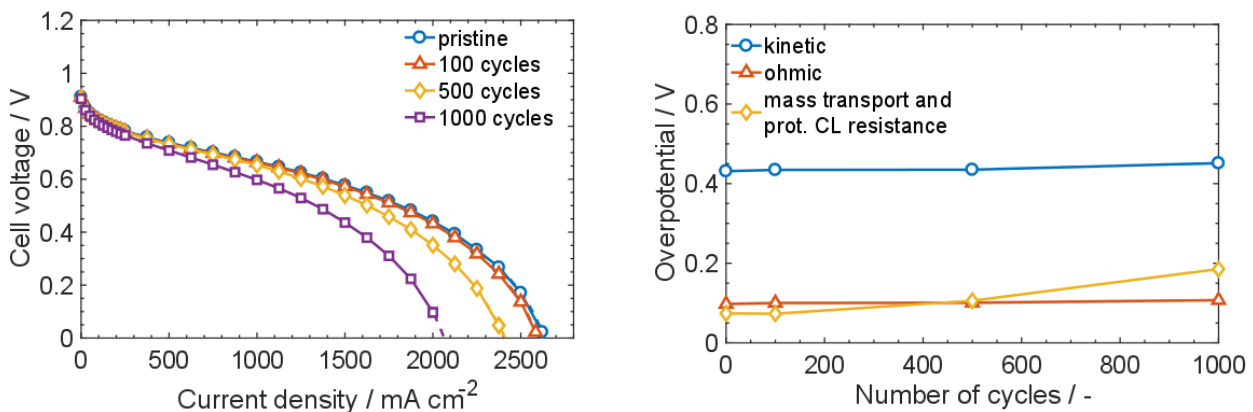


Figure 2: Performance loss (left) and overpotentials analysed by their origin (right)

As displayed in Figure 2, the kinetic and ohmic overpotentials do not change significantly during ageing, whereas the combined MTR (mass transport resistance) and protonic resistance overpotential increases over the ageing cycles. The protonic transport resistance is assumed to increase by a negligible amount as it decreases with the ionomer-to-carbon ratio^[5] induced by the carbon loss. Thus, the increased MTR overpotential is considered to account for the major part of the electrochemical performance loss. For this reason, the present investigations are focused on the increase of the MTR and how this is related to carbon corrosion.

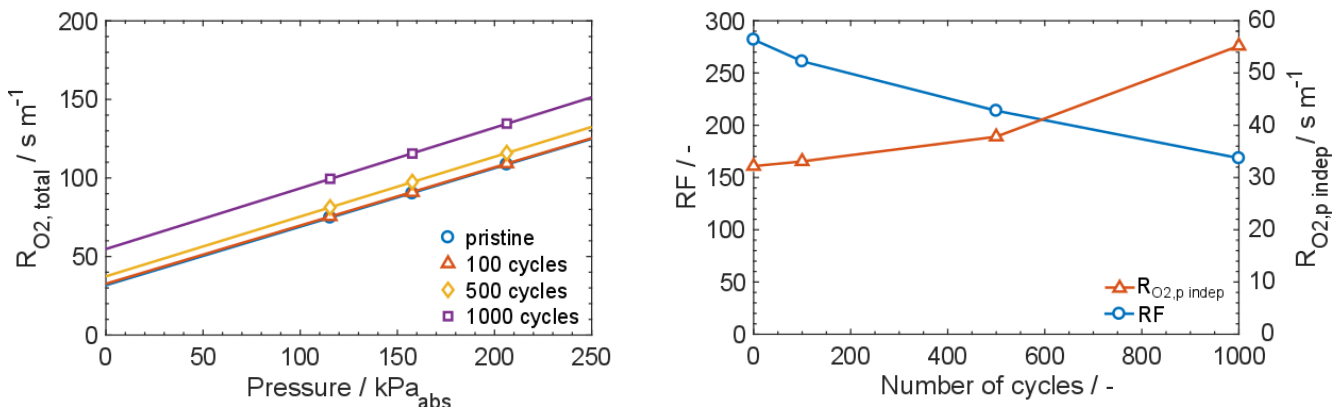


Figure 3: O₂ mass transport resistance vs. absolute pressure (left), and pressure independent MTR and roughness factor (RF) vs. ageing cycles determined by H₂ pumping experiments (right)

Measuring the limiting current in the H₂ pumping setup, described in Section 3.4, allows determination of the oxygen MTR without the effect of liquid water in the pore space, as described by Spingler et al.^[4]. By varying the pressure, the MTR can be divided into a pressure dependent part $R_{O_2,p}$ (Laplace gas diffusion in pore space) and a pressure independent part $R_{O_2,p\,indep}$ (interfacial resistance, diffusion resistance $R_{Cat,Local,surf}$ of the ionomer film covering the platinum catalyst and Knudsen diffusion). If Knudsen diffusion in the catalyst layer (CL) pores is neglected, $R_{CL,indep}$ is inversely proportional to the active surface area.

$$R_{O_2,p\,indep} = \frac{1}{RF} R_{Cat,Local,surf} + R_{O_2,CL,Knudsen}$$

As depicted in Figure 3 left, $R_{O_2,p}$ represented by the slope of the total MTR over the absolute pressure does not significantly change after ageing. Hence, nearly all of the MTR increase is due to an increase of $R_{O_2,p\,indep}$, displayed by the Y-axis intercept in Figure 3 (left) and versus the number of ageing cycles in Figure 3 (right). Assuming a constant $R_{Cat,Local,surf}$, the increase of $R_{O_2,p\,indep}$ and thus MTR is attributed to a loss of roughness factor RF (i.e. active surface area). This prediction is investigated with the simulation model described below.

4.1.2 STRUCTURAL CHANGES

Acquisition of tomographic images after the different ageing amounts (pristine, 100, 500, 1000 cycles) allowed changes in the microstructure of the catalyst layer to be investigated as shown in Figure 4, left.

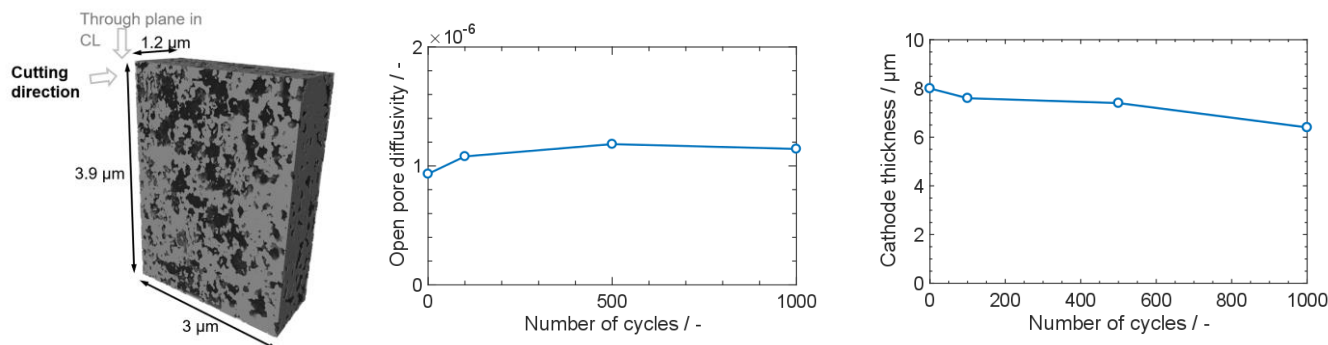


Figure 4: Example tomographic dataset (left), effect of cycling on pore diffusivity (centre) and effect of cycling on cathode catalyst layer thickness (right)

The diffusivity of the open pore space, i.e. without liquid water in the pore space, only changes slightly as shown in Figure 4, centre. First, it increases due to an increase in porosity then, after 500 cycles, a minor decrease of porosity and thereby diffusivity is observed, which is in agreement with Fuller et al.^[6]. This behavior can be explained by hollowing of the porous carbon support due to a loss of carbon, and subsequently a partial collapse of the weakened carbon support. However, since the change of diffusivity of the pore space is only minor, it is not considered to have a significant impact on the performance loss and the change in CL thickness is rather small (see below).

4.2 GENERAL DESCRIPTION OF THE MODEL

The model is zero-dimensional, but it integrates transport parameters calculated from 3D structures. In the following section the main equations for the model are described briefly:

The performance, i.e. the voltage as a function of the current density, can be described as the equilibrium potential minus the losses:

$$U(i) = E_0 - \eta_{kin}(i) - \phi_{ohmic} * i - \eta_{MTR}(i)$$

representing the kinetic, ohmic and mass transport losses. The model maps the influence of factors, such as porosity or ionomer film thickness, onto the MTR overpotential η_{MTR} . By definition, the MTR causes an effect on the reactant concentration, which can be linked to the concentration overpotential via the Nernst and the Butler-Volmer (BV) equation:

$$\eta_{MTR,Nernst} = \frac{RT}{4F} \ln\left(\frac{c_{O_2,chan}}{c_{O_2,cat}}\right)$$

$$\eta_{MTR,BV} = \frac{RT}{\alpha 4F} \ln\left(\frac{c_{O_2,chan}}{c_{O_2,cat}(1 - s_{CL})}\right)$$

with the oxygen concentration $c_{O_2,cat}$ corrected for the water saturation s_{CL} in the catalyst layer according to O'Hayre^[7].

The oxygen concentration at the catalyst particle surface depends on the diffusion through the ionomer film and the equilibrium concentration at the film surface:

$$c_{O_2,cat} = c_{O_2,eq} - j_{O_2} R_{O_2,film}$$

with the oxygen molar flux being

$$j_{O_2} = \frac{i}{4F}$$

and the diffusive resistance

$$R_{O_2,film} = \frac{1}{RF} \left(\frac{t_{film}}{D_{film}} + R_{O_2,if} \right)$$

as a combination of a bulk resistance and an interfacial resistance $R_{O_2,if}$ as described by Nonoyama et al. ^[8]. The interface resistance was taken from K. Kudo et al ^[1] and takes into account the interface between the ionomer film and the pore space above it and the interface between the ionomer and Pt underneath the ionomer. Importantly, to relate $R_{O_2,film}$ to the cell area, it needs to be divided by the roughness factor RF.

The oxygen concentration at the ionomer film outer surface is in equilibrium with the gas concentration and, therefore, can be calculated as:

$$c_{O_2,eq} = \frac{p_{O_2,CL}}{H}$$

with H being the Henry constant.

The oxygen partial pressure depends on the diffusion through the catalyst layer

$$p_{O_2,CL} = \frac{-j_{O_2} R T t_{CL}}{D_{O_2,CL} (s_{H_2O,CL})} + p_{O_2,GDL}$$

and through the gas diffusion layer (GDL)

$$p_{O_2,GDL} = \frac{-j_{O_2} R T t_{GDL}}{D_{O_2,GDL} (s_{H_2O,GDL})} + p_{O_2,chan}$$

and the respective partial pressures. The diffusivities, however, are functions of the liquid water saturation s_{H_2O} . For the CL, the diffusivity has been calculated for different liquid water saturations in Geodict and linearly interpolated between the calculated values. For the GDL, the relation

$$D = D_0 \varepsilon^{3.6} 0.7 (1 - s)^3$$

according to Weber et al. [9] has been applied, with the diffusivity D_0 and porosity ε coming from the tomography data (compare Section 4.1.2).

Since the oxygen and water transport both determine the liquid saturation s and the molar flux, the liquid saturation in the CL and GDL have to be determined iteratively. For this, the phase of the water and thus the mode of water transport, diffusion or permeation, has to be determined. To this end, the water partial pressure is determined with the same formula as the oxygen partial pressure and then compared to the saturation pressure:

$$p_{H_2O,sat} = 10^{10.1962 - \left(\frac{1730.63}{T - 39.7235}\right)}$$

as a function of the temperature according to the Antoine equation.

If the partial pressure exceeds the saturation pressure, liquid water is present and, as well as gaseous water vapour diffusion, permeation in the liquid phase is considered as a mode of water transport. The capillary pressure, i.e. the difference between liquid phase pressure and gas pressure

$$p_c = p_{H_2O} - p_g$$

is calculated by the Darcy transport equation for the liquid water

$$\Delta p_{H_2O} = q_{H_2O} * t * \frac{\mu_{H_2O}}{\kappa_{H_2O}(s)}$$

with the dynamic viscosity μ_{H_2O} , the thickness t , the intrinsic permeability κ_{H_2O} and the water volume flow, which is directly dependent on the generated water and therefore on the current density,

$$q_{H_2O} = \frac{i}{2F} \frac{M_{H_2O}}{\rho_{H_2O}}$$

with ρ_{H_2O} and M_{H_2O} being the density and molar mass of water respectively. The capillary pressure then yields the level of saturation through the capillary-pressure-saturation curves calculated from the pore size distribution (PSD) from the tomography data and the Young Laplace equation:

$$p_c = \frac{4 \gamma \cos\theta}{D}$$

with θ being the contact angle, the surface tension γ and the pore diameter D .

$$s = f(p_{cap})$$

The permeability is a function of the saturation and calculated by

$$\kappa_{H_2O}(s) = K s^2$$

according to Ramos-Alvarado et al. ^[10] with a material dependent constant K .

The model does not use any fitting parameters and is thus exclusively based on physical parameters and relations.

4.3 MODEL RESULTS: MTR AS A FUNCTION OF LAYER PARAMETERS

In this section, each of the potential changes is examined to assess their impact on performance (sensitivity analysis).

4.3.1 PORE SPACE (TORTUOSITY, POROSITY, THICKNESS)

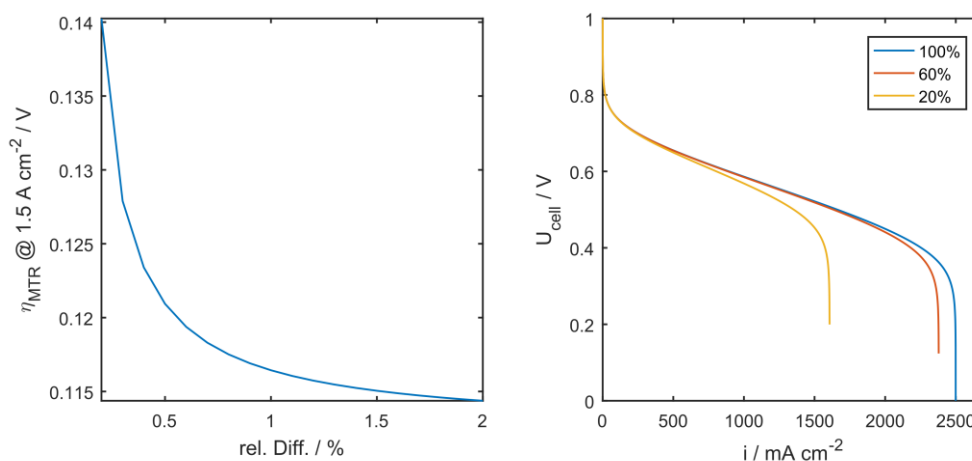


Figure 5: Sensitivity of the MTR overpotential to relative diffusivity (left), and simulated polarisation curves for different relative diffusivities (right)

As can be seen in Figure 5 the diffusivity in the pore space has a minor effect on the MTR and thus also on performance (right). The diffusion has to be hindered strongly (e.g. reduced to 20% of the initial value) in order to reduce the voltage significantly.

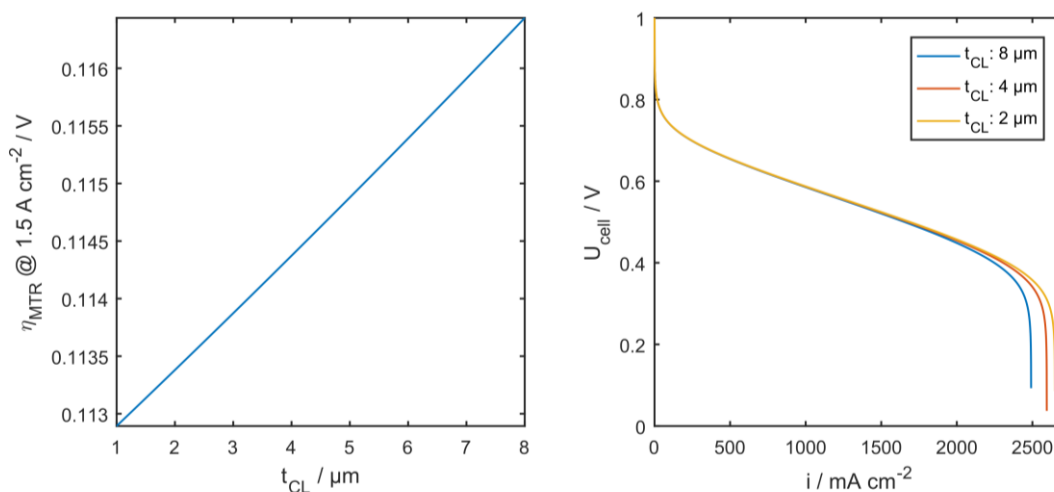


Figure 6: Sensitivity of the MTR overpotential to CL thickness (left), and simulated polarisation curves for different CL thicknesses (right)

As can be seen in Figure 6, the thickness of the CL has a positive linear correlation with the MTR overpotential such that with decreasing CL thickness the MTR also decreases. The linear correlation comes from the Fickian gas diffusion in the CL pores, which linearly correlates with the distance. However, since the gas diffusive resistance of the CL pore space only plays a minor role, CL thickness has only a minor effect on polarisation.

4.3.2 ECSA Loss

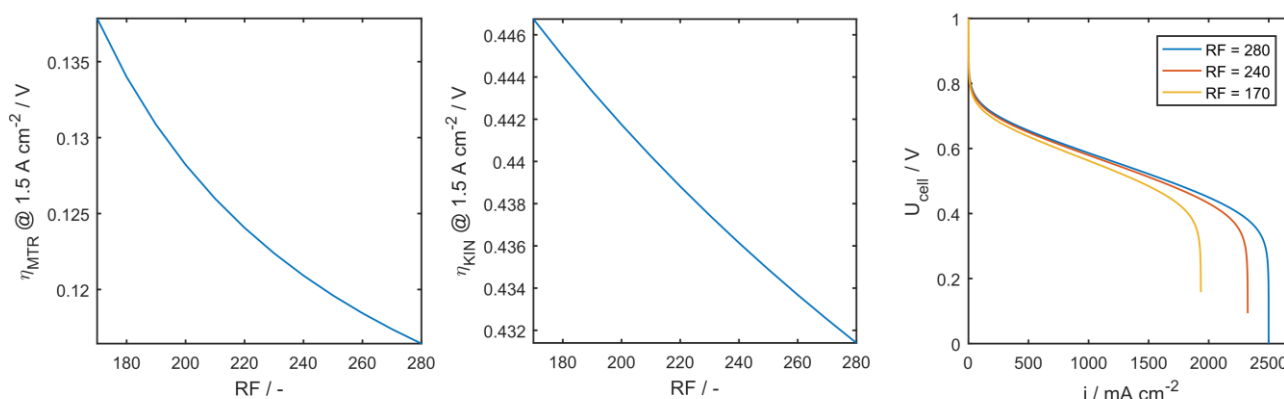


Figure 7: Sensitivity of the MTR overpotential to roughness (left), sensitivity of the kinetic overpotential to roughness (centre) and simulated polarisation curves for different roughness factors (right)

As can be seen in Figure 7, left, the MTR overpotential correlates strongly with the roughness factor (electrochemical surface area) consistent with the data calculated from the experimental results (Figure 3, right). The reason for this strong correlation lies in the large overpotential contribution from the local mass transport resistance, as described in Section 4.1.1. It should be noted that the reduced catalyst surface area (RF) also causes a small increase in the kinetic overpotential as displayed in Figure 7, centre.

4.3.3 WETTING BEHAVIOR: CONTACT ANGLE

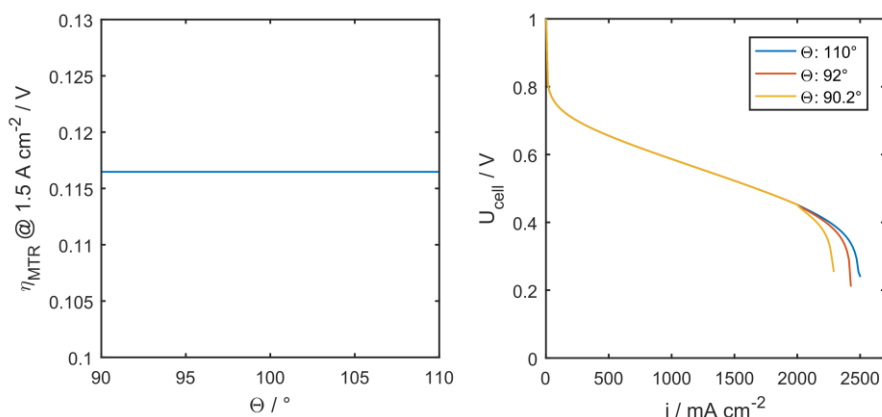


Figure 8: Sensitivity of the MTR overpotential to contact angle (left), and simulated polarisation curves for different contact angles (right)

As shown on the left of Figure 8, the modelled MTR overpotential at the DOE reference current density is not dependent on the CL wetting angle, due to the following reason: below a current density of approximately 2 A/cm^2 the water is diffusively transported in the gas phase without over-saturation. In this model, liquid water in the CL pores only exists at higher current densities ($> 2 \text{ A/cm}^2$). However, the Darcy transport of liquid water only requires small differential pressures correlating with a small capillary pressure and thus a minor liquid saturation. Therefore, a change of the performance (Figure 8, right) is only seen when the contact angle is close to 90° , i.e. when the required capillary pressure for water penetration is very low. It is noted, however, that a real CL does not exhibit a uniform contact angle and shows a range of hydrophobic contact angles and a few hydrophilic regions as well.

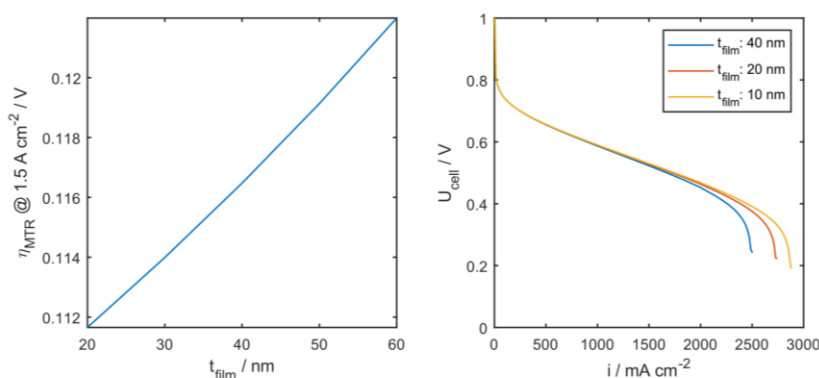


Figure 9: Sensitivity of the MTR overpotential to ionomer film thickness (left), cell potential curves for different ionomer film thicknesses (right)

4.3.4 IONOMER FILM THICKNESS

As can be seen in Figure 9 the MTR overpotential increases with ionomer film thickness. It is noted that the interfacial ionomer resistance corresponds to approximately 60 nm of film thickness according to Kudo et al ^[1]. Hence, the local mass transport is dominated by the interfacial resistance for thin ionomer films. It is not thought that the ionomer film reaches the values shown in Figure 9; typical ionomer film thicknesses are both calculated and measured to be between 3 and 5 nm on average.

4.4 VALIDATING THE MODEL

As depicted in Figure 10 (left) the inputs for modelling the performance degradation are the tomography data and the active surface area (roughness factor), obtained from CV measurements. With these input data, which have been measured for each ageing step, and the constant model parameters, the performance loss related to the observed catalyst degradation can be simulated. In the previous section, no correction factors were used to adjust the model. All the generated overpotentials and polarisation curves rely solely on physical parameters and relationships. The material properties are taken from experimental data in the literature. To validate the model, data from the experiments were used. The model is fitted to the pristine data, only by adjusting the prefactor of the Butler-Volmer-related mass transport overpotential and the OCV, while keeping all other parameters unaltered. The prefactor of the Butler-Volmer mass transport overpotential is often reported to be significantly higher than the theoretical $\frac{RT}{\alpha 4F}$ [7] and therefore adjusted, which yields a smoother transition from the Ohmic to the MTR region.

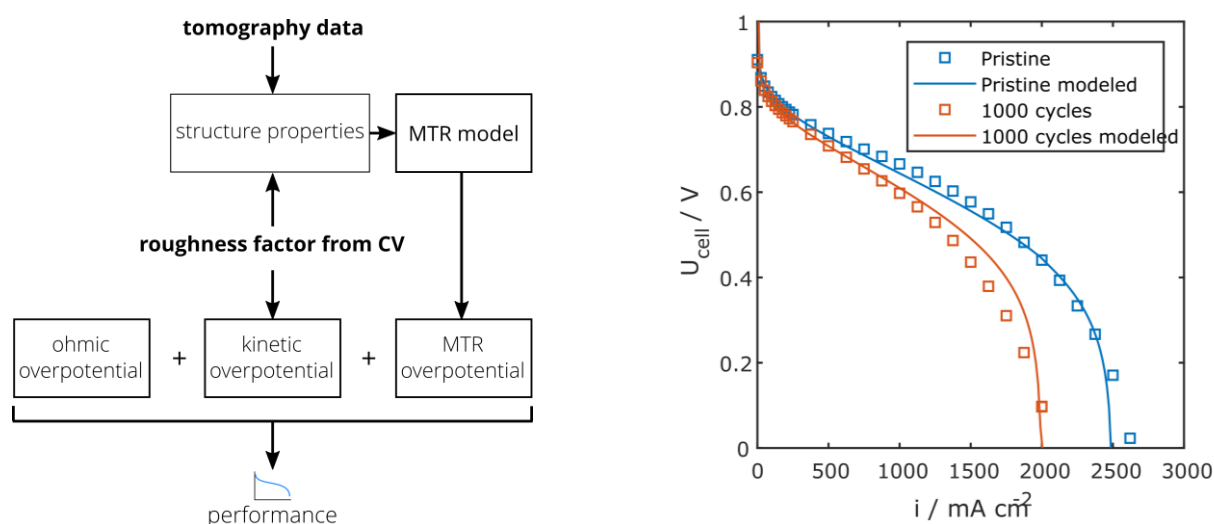


Figure 10: Set-up of the simulation model and input data (bold) for prediction of the performance degradation (left). Pristine and aged (1000 cycles) samples measured and modelled (right)

As can be seen in Figure 10 (right), the model predicts the pristine performance (blue) well. Finally, to validate the model, the parameters listed in Table 1 were fed into the model and the polarisation curve for the 1000 cycles aged sample predicted (orange). These parameters reflect the structural changes of the CL support, as calculated from the tomography data (CL thickness, diffusivities) and the loss of active surface area, as determined in CV measurements (roughness). It can be observed that the predicted polarisation curve fits the experimental data quite well.

Table 1: Input values for the model

| Parameter | Pristine | 1000 C |
|--------------------------|-----------------|-------------------|
| Roughness | 280 | 170 |
| Catalyst layer thickness | 8 μm | 6.4 μm |
| Laplace diffusivity | 0.1755 | 0.1764 |
| Knudsen diffusivity | 0.1395 | 0.1814 |

5 CONCLUSIONS

The model presented here is simple to use, whilst containing the necessary relationships to reliably predict the impact of several ageing mechanisms on performance. In the validation section, it was demonstrated that the model yields a very good prediction of performance decay, using tomographic and CV data as inputs. The major contributor to the performance loss is the increased mass transport resistance due to a loss of active Pt surface area. This finding is predicted by the model and was confirmed in the experimental data. The data shows that carbon corrosion undercuts the Pt nano-particles, detaching them from the carbon support and rendering them electrochemically inactive.

Prior studies on the structural changes in the catalyst layer induced by ageing and their effect on performance have investigated severely degraded catalyst layers. In the previous work, the catalyst layer showed a significant loss of porosity and diffusivity. However, the degradation was far beyond the expected ageing for normal operating conditions. This work, therefore, presents the more realistic impact of degradation mechanisms in the case of performance losses of about 30-50 mV @ 1.5 A/cm².

6 RECOMMENDATIONS AND FUTURE WORK

A key finding of this work is that loss of ECSA is the main reason for performance degradation in these tests, rather than collapse of the layer structure. This means that within this potential regime, new catalysts and supports can be screened by their resistance to ECSA loss when cycled between 1.0 and 1.5 V. Such a test can now be used to rank new materials being made within the INSPIRE project.

It should be noted that the model developed cannot account for all situations and a good understanding of the underlying assumptions and relationships will always be required and validation by testing and characterisation should support the use of the model.

7 REFERENCES

- [1] K. Kudo, R. Jinnouchi, Y. Morimoto, *Electrochimica Acta* **2016**, 209, 682.
- [2] US DOE **2017**.
- [3] J. Becker, A. Wiegmann, B. Planas, *DiffuDict: Release 2017* **2017**.
- [4] F. B. Spingler, A. Phillips, T. Schuler, M. C. Tucker, A. Z. Weber, *International Journal of Hydrogen Energy* **2017**, 42, 13960.
- [5] Y. Liu, M. Murphy, D. Baker, W. Gu, C. Ji, J. Jorne, H. A. Gasteiger, in *ECS Transactions*, ECS **2007**, p. 473.
- [6] A. G. Star, T. F. Fuller, *J. Electrochem. Soc.* **2017**, 164, F901-F907.
- [7] R. O'Hayre, S.-W. Cha, F. B. Prinz, W. Colella, *Fuel cell fundamentals*, John Wiley & Sons **2016**.
- [8] Nobuaki Nonoyama, Shinobu Okazaki, Adam Z. Weber, Yoshihiro Ikogi, *J. Electrochem. Soc.* **2011**, 158, B416-B423.
- [9] A. Z. Weber, R. L. Borup, R. M. Darling, P. K. Das, T. J. Dursch, W. Gu, D. Harvey, A. Kusoglu, S. Litster, M. M. Mench, R. Mukundan, J. P. Owejan, J. G. Pharoah, M. Secannel, I. V. Zenyuk, *J. Electrochem. Soc.* **2014**, 161, F1254-F1299.
- [10] B. Ramos-Alvarado, A. Hernandez-Guerrero, D. Juarez-Robles, P. Li, *International Journal of Hydrogen Energy* **2012**, 37, 436.